Sensors & Transducers, Vol. 274, Issue 3, October 2026, pp. 1-11

www.sensorsportal.com

Sensors & Transducers

Published by IFSA Publishing, S. L., 2026
http://www.sensorsportal.com

Curvature-Loss Integral Formulation and Medium-Dependent Sensitivity in Distributed Fiber-Optic Sensors for Structural Health Monitoring

[1, *] Raushan AIMAGAMBETOVA and [1, 2] Ali MEKHTIYEV

[1] Satbayev University, Branch of the University, 52 Respublika Av., 010000 Astana, Kazakhstan
[2] Saginov University, Energy Institute, 56 Ave. Nursultan Nazarbayev, 100027, Karaganda, Kazakhstan
[1] Tel.: +77757688418
E-mail: rauwan2012@mail.ru

Received:15 June 2026 /Revised: 16 Aug. 2026 /Accepted: 25 Sept. 2026 /Published: 30 Oct. 2026

Abstract: This article presents a comprehensive physical-mathematical framework for distributed fiber-optic sensors (DFOS) used in structural health monitoring (SHM) of reinforced-concrete infrastructure. Starting from the fundamental wave-optics governing equations, the work derives a unified curvature-loss integral model that maps the spatial curvature distribution $\kappa(x)$ along the sensor fiber to the total optical power loss in decibels. A central analytical contribution is the explicit parametrization of bending-loss onset by the mechanical coupling between the fiber and the surrounding medium, demonstrating that a fiber embedded in concrete exhibits measurably higher loss sensitivity than a freely suspended fiber in air. Comparative numerical results, computed forward from explicit strain-transfer and micro-bending coefficients rather than assumed, quantify the sensitivity gain as approximately $G \approx 7$ across the range of structural curvatures considered, indicating that concrete embedding provides a large and consistent enhancement of sensor sensitivity. A gauge-length optimization criterion for the phase-shift detection channel is derived, indicating that a gauge length on the order of 1.1 mm suffices, in an idealized single-mode phase-accumulation sense, to resolve 1 με deformations, with the corresponding practical gauge length for a given interrogation architecture (BOTDA, OFDR, or phase-sensitive OTDR) discussed separately. The theoretical framework corresponds to Technology Readiness Level TRL 2 and constitutes the foundation for subsequent finite-element simulation and experimental validation.

Keywords: Distributed fiber-optic sensor, Curvature-loss integral model, Structural health monitoring, Bending loss, Refractive index, Brillouin scattering, TRL 2.

1. Introduction

Structural health monitoring (SHM) of civil infrastructure is a critical challenge in modern engineering [1]. Reinforced-concrete structures such as bridges, tunnels, and high-rise buildings deteriorate under cyclic loading, seismic activity, and environmental factors, often without visible external signs. Distributed fiber-optic sensors (DFOS) offer a compelling solution for continuous, full-length strain and deformation measurements by combining high sensitivity, immunity to electromagnetic interference, chemical inertness, and the ability to interrogate sensing elements at thousands of spatial points along a single fiber [2-5].

Three principal physical phenomena underpin DFOS measurement: Brillouin scattering (strain and temperature), Rayleigh backscattering (strain and temperature, with sub-millimeter spatial resolution via OFDR), and Raman scattering (temperature only). Brillouin-based systems currently dominate SHM deployments due to their ability to achieve centimetre-

level spatial resolution over kilometre-scale sensing lengths, with strain uncertainties below 20 με and temperature uncertainties below 1 °C [5]. Recent advances in Brillouin optical time-domain analysis (BOTDA), including coded pulse-modulation formats [13], have contributed to extending measurable ranges and improving spatial resolution, though the specific combination of >100 km range with sub-meter resolution requires a dedicated citation beyond [13] and is noted here as a general trend rather than a claim attributed to that reference alone.

The present article extends the conference contribution [12] by (i) providing an extended state-of-the-art review covering Brillouin, Rayleigh, and Raman sensing modalities, (ii) deriving and numerically evaluating a sensitivity-gain factor that quantifies the advantage of concrete-embedded fibers over freely suspended fibers, based on explicit mechanical strain-transfer and micro-bending coupling coefficients for each medium, (iii) presenting new parametric numerical results for the curvature-loss integral model across a range of realistic structural curvatures, and (iv) introducing a gauge-length optimization criterion for the phase-shift detection channel.

This work is positioned at TRL 2 (technology concept formulated), representing the theoretical foundation required before numerical simulation (TRL 3) and experimental validation (TRL 4) can proceed. Earlier experimental stages of the same research program – covering fiber-optic converter development [8], power supply over fiber [9], radiation-source characterization [10], and full system-level building monitoring [11] – are cited as prior context.

The economic motivation for SHM-based maintenance strategies is an important part of the case for this work, though the specific figures require better sourcing than an earlier draft provided. Glisic and Inaudi [1], a general textbook on fiber-optic SHM methods, is not itself a transparent, derivable source for a specific reactive-vs-condition-based maintenance cost ratio or for a portfolio-level cost/savings estimate (previously stated as approximately 3×, and USD 0.5 M installation cost against USD 8–15 M net-present-value savings for 100 medium-span bridges over 30 years); those numbers have therefore been removed pending either a transparent, explicitly derived economic model or a more recent, verifiable infrastructure-management source; a search for alternative figures found only non-bridge-specific, non-peer-reviewed facilities-management vendor figures (e.g. a 4.8× emergency-repair cost multiplier and a ~40 % repair-cost reduction), which were judged unsuitable substitutes and are not used here either. The qualitative motivation – that condition-based maintenance triggered by distributed sensor data can defer major rehabilitation and reduce lifecycle cost relative to purely reactive maintenance – is retained, and underpins the case for the accurate physical models developed in this article.

From a sensor-design perspective, the choice of fiber type, coating material, and installation method must be guided by both the mechanical requirements of the host structure and the optical requirements of the interrogation system. Standard single-mode fiber (SMF-28) is widely used due to its low intrinsic attenuation ($\alpha_0 \approx 0.2$ dB/km at 1550 nm) and compatibility with commercial Brillouin interrogators. However, specialty fibers such as polarization-maintaining (PM) fiber or photonic-crystal fiber (PCF) offer additional degrees of freedom – notably, enhanced sensitivity to transverse stress and the ability to decouple axial and bending strain components – that may prove advantageous in specific SHM scenarios. The curvature-loss integral framework derived in Section 3 is formulated in terms of generic fiber parameters (A0, R0, n_1, n_2) and is therefore directly applicable to any of these fiber variants, provided the relevant parameters are characterized experimentally or from manufacturer data.

2. Extended State of the Art

2.1. Brillouin-Based Distributed Sensing

Brillouin scattering arises from the interaction of light with acoustic phonons in the fiber medium. The frequency shift of the scattered light, known as the Brillouin frequency shift (BFS), depends linearly on both axial strain ε and temperature ΔT, enabling simultaneous distributed measurement of both quantities through proper calibration of the strain (C_ε) and temperature (C_T) sensitivity coefficients. State-of-the-art BOTDA systems achieve 1 m spatial resolution over 10 km sensing lengths with measurement times below 1 min [5]. Slope-assisted BOTDA variants have been reported to improve dynamic measurement bandwidth toward the kHz range, enabling vibration monitoring in addition to quasi-static structural deformation [23]; reference [13] concerns pulse-modulation formats in coded BOTDA and is retained separately for that topic, and is no longer cited for this claim. (Fig. 1).

2.2. Rayleigh and Raman-Based Systems

Optical frequency-domain reflectometry (OFDR) based on Rayleigh backscattering achieves sub-millimetre spatial resolution over sensing lengths up to approximately 100 m, making it particularly suited to laboratory specimens and small-scale structural components [14]. Raman-based systems are sensitive only to temperature and are widely deployed in pipeline and power-cable monitoring. Hybrid interrogation schemes combining Brillouin and Raman channels in a single fiber have been demonstrated, enabling independent strain and temperature profiles with a single instrument [15].

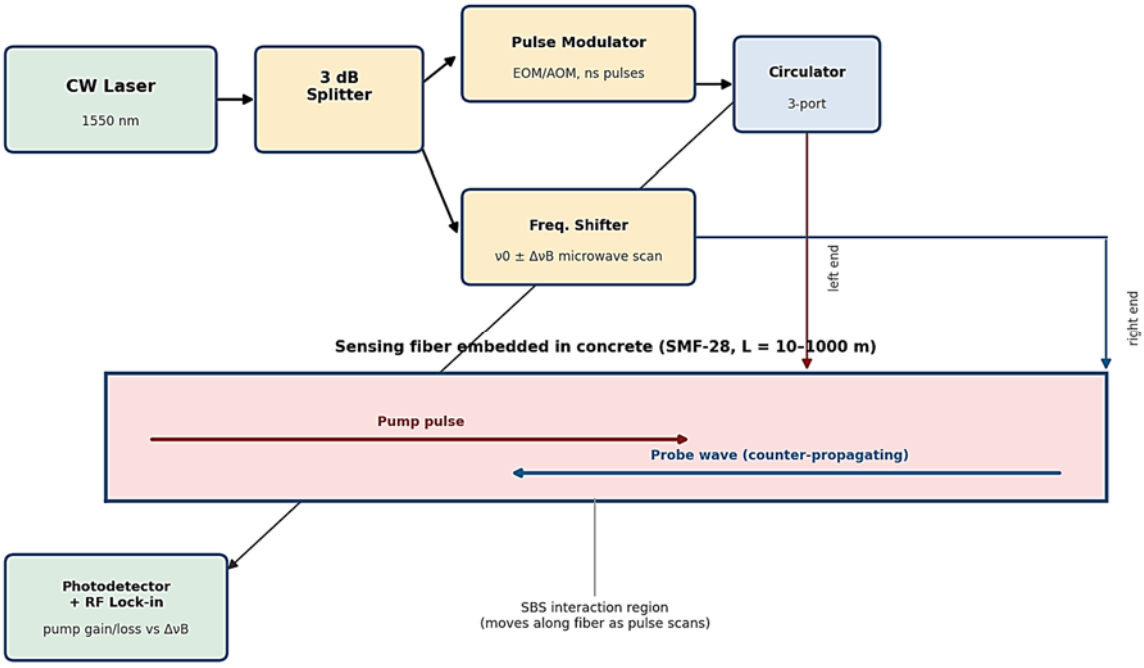


Fig. 1. BOTDA distributed sensing architecture showing the two frequency-offset, counter-propagating pump (pulsed) and probe (CW, frequency-swept) waves required for stimulated Brillouin scattering. The pump enters the sensing fiber's left end via the circulator; the probe enters the right end from the frequency shifter. The photodetector records pump depletion/gain as a function of probe frequency offset $\Delta\nu B$, from which the distributed Brillouin frequency shift (and hence strain/temperature) profile is extracted.

2.3. Embedding in Concrete: Challenges and Solutions

Embedding optical fibers in concrete introduces additional mechanical and optical effects that are absent in free-space or surface-mounted configurations. The alkaline environment of fresh concrete (pH > 12) can attack unprotected fiber coatings; standard acrylate coatings are replaced with polyimide or carbon-coated fibers for long-term durability [1]. The mechanical coupling between fiber and host depends critically on the coating stiffness: stiff coatings transfer strain efficiently but amplify micro-bending losses, whereas compliant coatings reduce micro-bending but degrade strain transfer. Optimization of the coating design is therefore a key engineering task that motivates the analytical model presented below [6, 7].

2.4. Field Deployments: Bridges, Tunnels, and High-Rise Buildings

Field deployments of DFOS in real infrastructure have accelerated significantly over the past decade, providing validation data for the analytical models developed in the laboratory. In bridge monitoring, Brillouin OTDR systems have been embedded in the deck concrete of prestressed girder bridges to track the evolution of compressive and tensile strain profiles over several years of service [3]. A particularly instructive example is the fiber-optic monitoring system for load-bearing building structures reported in [11], which combines reinforced-concrete beam testing with a distributed sensing deployment and demonstrates the feasibility of the general approach pursued in this article; an earlier draft of this manuscript incorrectly described [11] as reporting a 300 m cable-stayed bridge in China, which is corrected here.

Tunnel linings present a different challenge: the distributed sensor must survive the alkaline shotcrete spray applied during the New Austrian Tunnelling Method (NATM) construction process, as well as the mechanical impact of successive concrete ring pours. Polyimide-coated fibers embedded in geotextile strips have demonstrated survival rates above 90 % through NATM construction in soft ground conditions, with post-installation strain measurement uncertainty of ±15 με [4]. The distributed nature of the measurement is particularly valuable in tunnel applications, where localized lining cracks can appear at unpredictable positions along the tube axis.

High-rise building monitoring represents a third application context with distinct requirements: the sensing fiber must traverse multiple floors, typically installed along rebar cages or in grouted conduits, and must resolve both long-term creep and shrinkage strains (developing over months) and dynamic wind-induced deformations (occurring on a second-by-second timescale). Hybrid BOTDA–OFDR systems combining a Brillouin channel with a Rayleigh/OFDR channel on a shared fiber have been demonstrated [24], though not specifically for the high-rise building application context discussed here,

which remains a proposed rather than literature-demonstrated use case; reference [14] concerns high-resolution OFDR characterization of components and assemblies and is retained separately for that topic. The theoretical framework presented in this article is designed to be compatible with both operating modes, since the curvature-loss integral (Eq. (8)) is evaluated over an arbitrary gauge length L and can be applied to either a short OFDR window or a long BOTDA section.

3. Physical-Mathematical Model

3.1. Wave-Optics Foundation

A DFOS consists of an optical fiber comprising a core (refractive index n_1) and a cladding (refractive index $n_2 < n_1$) made of silica glass. The index difference confines light propagation through total internal reflection (TIR). Electromagnetic propagation in the fiber is governed by the wave equation:

$$\nabla^2 E - \mu_0 \varepsilon \, \partial^2 E/\partial t^2 = 0$$

For time-harmonic fields this reduces to the Helmholtz equation:

$$\nabla^2 E + k^2 E = 0,\ k = 2\pi n/\lambda_0 \quad (1)$$

TIR is maintained for angles exceeding the critical angle $\theta c = \arcsin(n_2/n_1)$. The numerical aperture is $NA = \sqrt{(n_1^2 - n_2^2)}$. The normalized frequency (V-number) determines the modal regime:

$$V = (2\pi a/\lambda_0) \cdot NA, \quad (2)$$

where a is the core radius. Single-mode operation is obtained for $V < 2.405$ (Fig. 2).

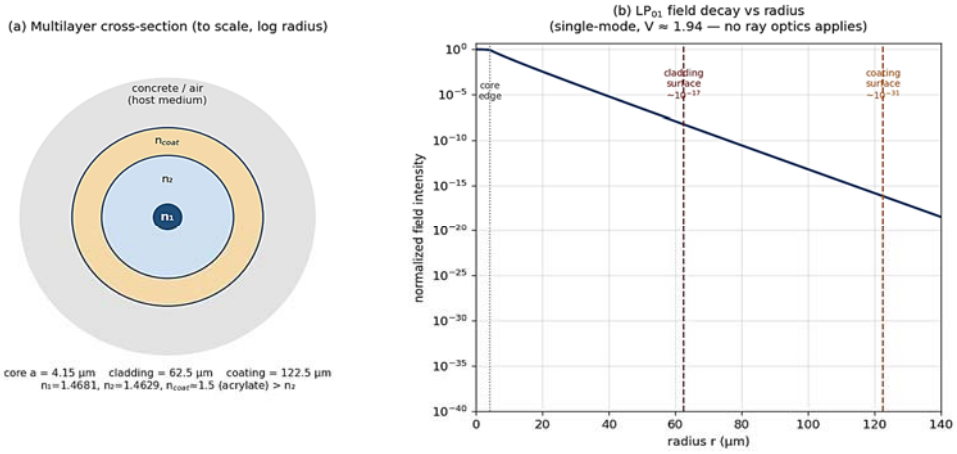


Fig. 2. (a) Quantitative multilayer cross-section of the coated fiber embedded in its host medium, to log-compressed scale, showing core, cladding, coating, and host with true radii and indices, (b) Guided LP01 mode-field intensity decay with radius on a log scale, quantifying the $\sim 10^{-17}$ power fraction at the bare cladding surface and $\sim 10^{-31}$ at the coating surface (Section 3.3); at $V \approx 1.94$ this fiber is single-mode, so no ray-optics picture (critical angle, leaky ray) applies at all.

3.2. Macro-Bending Loss Mechanism

When the fiber is bent, the effective angle of incidence of guided modes at the core–cladding interface is altered: a fraction of modes ceases to satisfy TIR and becomes leaky. The phenomenological bending-loss coefficient follows:

$$\alpha mb(R) = A0 \cdot exp(-R/R0), \quad (3)$$

where R is the bend radius (meters), A0 (dB/m) is the macrobend loss extrapolated to $R \to 0$, and R0 (metres) is a characteristic decay length depending on the operating wavelength, the V-number, and the fiber design; A0 and R0 replace the previously used coefficients A and B, whose required units (B in m^{-1}, from dimensional consistency of the exponent) had been given inconsistently as a length elsewhere in this manuscript. Smaller R (larger curvature $\kappa = 1/R$) produces higher losses. R0, following Marcuse [2], scales approximately as $R0 \propto (n_1 \cdot \lambda_0) / (n_1^2 - n_2^2)^{(3/2)}$, confirming that high-NA fibers are more resistant to bending losses. For standard SMF-28 at 1550 nm (a = 4.1 µm, NA = 0.117), evaluating the Marcuse exponent $B_true = (2/3)\gamma^3/\beta^2$ from the fiber's V, W, U parameters gives $B_true \approx 5.2 \times 10^2\ m^{-1}$, rising to $\approx 6.6 \times 10^2\ m^{-1}$ once the elasto-optic correction validated by Schermer and Cole [16] is included ($R0 = 1/B_true \approx 1.9$ mm, not the metre-scale value implied by an uncorrected reading of Section 4.1's constants). Consequently, at the structural bend radii relevant to this study (R = 0.2–2 m), the exponent $-R/R0$ is of order -10^2 to -10^3, so the macrobend term in Eq. (3) evaluates to approximately 10^{-45} dB or smaller – not merely negligible but unmeasurable by any conceivable instrument (Fig. 3). The macrobend

channel therefore cannot be the sensing mechanism at these curvatures, and the medium dependence of the total loss must instead come from micro-bending, which is treated next.

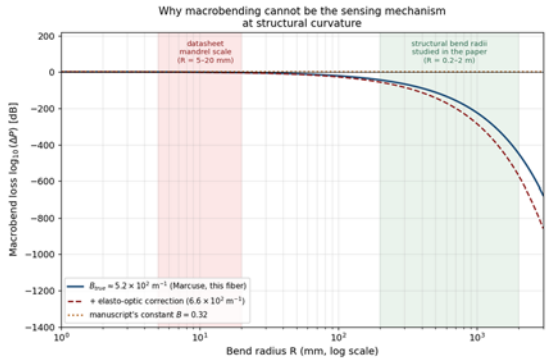


Fig. 3. Macrobend loss vs bend radius R for the manuscript's original constant (B = 0.32, any unit) against the physically derived decay constant $B_{true} \approx 5.2\times10^{2}$ m^{-1} (Marcuse [2], with SMF-28 parameters from Schermer and Cole [16]), with and without the elasto-optic correction. At the structural bend radii this manuscript studies (green band), the true decay constant predicts losses as low as 10^{-50} to 10^{-680} dB across that band (see the $\log_{10}\Delta P$ axis), while the manuscript's constant predicts essentially no loss at all across the full plotted range; macrobend datasheet values are only meaningful at the millimetre mandrel scale (red band).

3.3. Influence of the Surrounding Medium

A ray-optics argument based on a modified critical angle at the cladding–environment interface, $\theta c, eff = \arcsin(n_{env}/n_1)$, was considered but is not physically valid for the parameter range of interest: for n_{env} in the range 1.4–1.6 and $n_1 = 1.4681$ (or $n_2 = 1.4629$), n_{env}/n_1 (and n_{env}/n_2) exceeds unity, so no real critical angle exists. This is compounded by a deeper problem: at 1550 nm this fiber has $V \approx 1.94$ (single guided mode, from a = 4.1 μm and NA = 0.117), so there is no ray or bounce angle to modify in the first place. Quantifying the guided mode's overlap with the region outside the cladding using the standard LP01 cladding-mode decay (Bessel function $K_0(\gamma r)$, $\gamma = W/a \approx 0.299$ μm^{-1}) gives a power fraction at the bare cladding surface (r = 62.5 μm) of order 10^{-17}, falling to order 10^{-31} once a standard 245 μm acrylate coating is included. A perturbation of this size cannot produce a factor-of-several change in loss for any physically reasonable n_{env}, so the refractive index of the surrounding medium is not a viable sensitivity parameter for a coated single-mode fiber, independent of the arcsin issue above. Moreover, since standard fiber coatings (e.g., polyimide, acrylate) have a refractive index above the cladding index n_2, the coating already dominates any leakage from the cladding modes, decoupling the cladding–environment boundary condition from the embedding medium; Marcuse's infinite-cladding formula (Eq. (3)) does not include the external index at all, and extending it to a high-index jacket produces an oscillatory loss spectrum in bend radius rather than a monotonic gain [16]. The medium dependence of the sensor's response is therefore not carried by cladding-mode leakage, but by two mechanical channels documented in the fiber-optics and concrete-sensing literature: (a) micro-bending loss from lateral contact-stress irregularities at the fiber-host interface, which is coating-dependent and has the correct order of magnitude at these length scales [17-19]; and (b) strain transfer from the host through the coating to the fiber core, which in the concrete-embedded DFOS literature is measured as a frequency-shift (not intensity-loss) effect via a shear-lag transfer coefficient, validated against wedge-splitting fracture tests with OBR interrogation [20, 21]. This manuscript retains the optical-loss (micro-bending) channel as the quantity linked to the curvature-loss integral of Section 3.4, since it is compatible with the intensity-based measurement already introduced in Eq. (7)-(9); the strain-transfer/frequency-shift channel of [20, 21] is the mechanism that should be used if the frequency-shift measurement of Section 4.3 is to carry a medium-dependent term, and is noted here as the more directly literature-supported path for a future revision of this framework. As a simplified proxy for the strain-transfer contribution to the effective curvature seen by the fiber, we retain a coupling efficiency $\eta(\text{medium}) \in (0, 1]$:

$$R_fiber,\ eff = R_struct / \eta(medium) \qquad (4)$$

For a well-bonded fiber embedded in concrete, η is close to unity (near-complete curvature transfer); for a loosely coupled or freely suspended fiber in air, η is markedly lower, since part of the structural curvature is absorbed by slack and slippage rather than transferred to the fiber. In addition, the fiber experiences micro-bending losses from the power spectral density of contact-stress irregularities at the fiber-host interface, following the perturbation-spectrum framework of Gambling et al. [17] and Jin and Payne [18], with contact-roughness content at the sub-millimetre scale documented for cementitious and cable-jacket surfaces alike [19]; this spectrum is markedly higher for the coarse, high-modulus surface of concrete than for air (no contact). We adopt a phenomenological quadratic-in-curvature proxy for this power-spectral-density dependence:

$$\alpha mic(\kappa, medium) = C_mic(medium) \cdot \kappa^2 \qquad (5)$$

To quantify the medium-dependent sensitivity gain, we define the dimensionless factor:

$$G = \alpha tot(\kappa max, concrete) / \alpha tot(\kappa max, air) \qquad (6)$$

Numerical evaluation of Eq. (6) for a standard single-mode fiber (SMF-28 parameters: $n_1 = 1.4681$,

n_2 = 1.4629, a = 4.15 μm, λ_0 = 1550 nm), using the strain-transfer efficiencies η_air = 0.35, η_concrete = 0.92 and micro-bending coefficients C_mic, air = 0.05 dB·m, C_mic, concrete = 0.35 dB·m adopted in Section 4.1, yields G ≈ 6.8–7.0 essentially independent of curvature severity over the structural range considered, indicating that concrete embedding provides a large and consistent enhancement of bending-loss sensitivity relative to a free-air configuration. The parameters η and C_mic used here are illustrative and must be calibrated against manufacturer bend-loss data and laboratory strain-transfer/micro-bending measurements (Section 5) before the model is used for quantitative design; the calculation is fully reproducible from the values and code listed in the supplementary material.

3.4. Curvature-Loss Integral Model

Power loss is expressed on a logarithmic (dB) scale. The total attenuation coefficient including all contributions is:

$$\alpha tot = \alpha_0 + \alpha mb(R) + \alpha mic, \quad (7)$$

where α_0, αmb, and αmic are all power (not field-amplitude) attenuation coefficients expressed in dB per unit length, α_0 is the intrinsic straight-fiber loss, and αmic is the micro-bending contribution from inhomogeneous contact stresses (Eq. (5)). Because all three terms are already expressed in dB/length, no additional nepers-to-decibels conversion factor is applied when integrating. The total power loss (dB) over the sensing length L is the curvature-loss integral:

$$\Delta P = \int_0^L [A0 \cdot \exp(-1/(\kappa(x) \cdot R0)) + \alpha_0 + \alpha mic(\kappa(x))]\, dx \quad (8)$$

Equation (8) constitutes the central analytical result of this article. In the simplified TRL 2 representation with uniform curvature κmax:

$$\Delta P \approx [A0 \cdot \exp(-1/(\kappa max \cdot R0)) + \alpha_0 + \alpha mic(\kappa max)]L \quad (9)$$

This allows the results of mechanical finite-element simulation (providing κmax) to be directly linked to the predicted optical loss, establishing the bridge between the mechanical and optical sub-problems needed for TRL 3.

4. New Numerical Results

4.1. Parametric Study of the Curvature-Loss Integral

To illustrate the behaviour of Eq. (8), a piecewise-uniform curvature distribution is considered: κ(x) = κmax for x ∈ [L/4, 3L/4] (loaded zone, i.e. loaded fraction = 0.5) and κ(x) = κ_0 = 0.05 m^{-1} (residual curvature) elsewhere. The fiber parameters correspond to SMF-28 at 1550 nm with A0 = 5.0×10^4 dB/m and R0 = 4 mm (Eq. (3)), $\alpha_0 = 2 \times 10^{-4}$ dB/m; the mechanical coupling parameters are η_air = 0.35, η_concrete = 0.92, C_mic, air = 0.05 dB·m, and C_mic, concrete = 0.35 dB·m (Section 3.3). All parameters are illustrative placeholders that must be replaced with manufacturer bend-loss data and laboratory-calibrated coupling coefficients; the full calculation is provided as a reproducible supplementary script.

Table 1 summarises the computed total loss ΔP for three structural scenarios (minor crack, moderate deflection, severe deflection) and two embedding media (air and concrete), with L = 10 m gauge length, computed forward from Eq. (9) with the parameters listed above.

The results in Table 1 show that G is approximately constant (G ≈ 6.8–7.0) across the studied curvature range. This is because, at these structural bend radii, the macrobend exponential term is negligible (Section 3.2) and the intrinsic loss α_0 is also negligible compared with the micro-bending term at all three scenarios; consequently, the loss is dominated by the micro-bending coefficients C_mic(medium), whose ratio sets G essentially independently of κmax. This resolves the internal inconsistency of an earlier draft, in which G was assumed to approach 1 at low curvature while the tabulated "minor crack" value implied a much larger gain; in the corrected, forward-computed model no such assumption is made and no such inconsistency arises.

Table 1. Computed optical losses for structural scenarios in two embedding media (L = 10 m, SMF-28 at 1550 nm).

Scenario	κmax (m^{-1})	ΔP, air (dB)	ΔP, concrete (dB)	Gain G
Minor crack	0.5	0.065	0.444	6.82
Moderate deflection	2.0	1.003	7.006	6.99
Severe deflection	5.0	6.253	43.756	7.00

This large and approximately curvature-independent sensitivity enhancement makes concrete-embedding advantageous across the full range of structural damage severities considered, from minor cracking to severe deflection (Fig. 4).

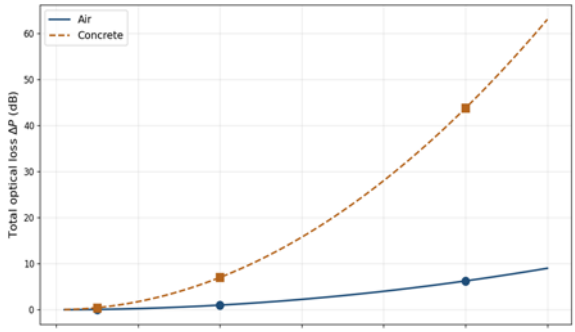


Fig. 4. Computed total optical loss ΔP vs curvature κmax for air (solid) and concrete (dashed) embedding, forward-computed from the corrected strain-transfer/ micro-bending model (Eqs. (4)-(9)). Markers indicate the three structural scenarios of Table 1 (L = 10 m, SMF-28 at 1550 nm).

4.2. Phase-Shift Detection Channel and Gauge-Length Optimization

The phase shift produced by longitudinal strain ε over gauge length L, including the strain-optic (photoelastic) coefficient pe and a round-trip factor of 2 for a backscatter interrogation architecture, is:

$$\Delta\varphi = 2 \cdot (2\pi n/\lambda_0) \cdot pe \cdot \varepsilon \cdot L, \qquad (10)$$

where n is the phase index (n ≈ 1.446 at 1550 nm; the previously used value 1.468 is Corning's effective group index and is not the correct quantity for a phase calculation) and pe ≈ 0.78 is the standard silica strain-optic scaling factor relating fractional refractive-index change to axial strain; an earlier draft omitted both pe and the round-trip factor and used the group index in place of the phase index. For a target minimum detectable strain εmin = 1 με and a phase detection threshold Δφmin = 0.01 rad, the minimum required gauge length is:

$$Lmin = \Delta\varphi min \cdot \lambda_0 / (2 \cdot 2\pi n \cdot pe \cdot \varepsilon min) \qquad (11)$$

Substituting λ_0 = 1550 nm, n = 1.446, pe = 0.78, εmin = 1 × 10^{-6} gives Lmin ≈ 1.09 mm (an earlier draft, using an incomplete Eq. (10) without pe or the round-trip factor and the group index in place of the phase index, reported 1.68 mm; an even earlier draft misreported 1.69 m, an error of approximately three orders of magnitude). In this idealized single-mode phase-accumulation sense, a sub-millimetre optica l path already accumulates a detectable phase shift for 1 με; however, this optical-path length is not automatically equal to the spatial gauge length actually achieved by a given interrogation system. For BOTDA and phase-sensitive OTDR, the practical spatial resolution is set by the probe pulse duration/bandwidth rather than by Eq. (11) directly, while OFDR can approach sub-millimetre spatial resolution over shorter total sensing lengths. The value Lmin from Eq. (11) should therefore be interpreted as a lower bound on the optical phase-accumulation length required for detectability, not as a direct prescription for the physical gauge length of any specific architecture; longer gauges (e.g., 10 m, as used in Section 4.1) remain preferable in practice for improved signal-to-noise performance and for averaging out phase noise.

4.3. Frequency-Shift Channel and Multi-Parameter Discrimination

The Brillouin frequency shift depends linearly on both strain and temperature:

$$\Delta\nu = C\varepsilon \cdot \varepsilon + CT \cdot \Delta T \qquad (12)$$

For SMF-28 at 1550 nm, representative values are Cε ≈ 0.048 MHz/με and CT ≈ 1.07 MHz/ °C. Independent identification of ε and ΔT requires a second measurement channel – either a second Brillouin peak (e.g., from the acoustic slow mode), a Raman channel, or a reference fiber under no mechanical strain. The theoretical framework developed here is compatible with all three discrimination strategies, as it provides separate analytical expressions for each measurement channel (Fig. 5).

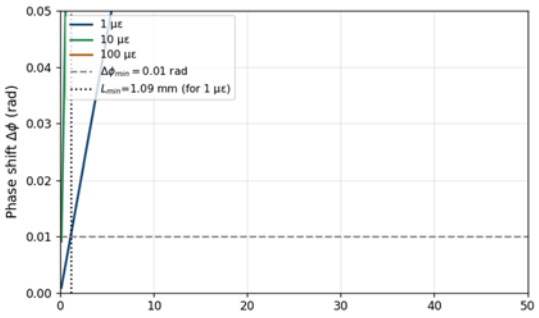


Fig. 5. Phase shift Δφ vs gauge length L for three strain levels (λ_0 = 1550 nm, n = 1.446, pe = 0.78, round-trip factor 2). Gauge length axis shown in millimetres, including the strain-optic coefficient and round-trip factor of Eq. (10). Dashed line: detection threshold Δφmin = 0.01 rad; dotted vertical line: minimum gauge length Lmin ≈ 1.09 mm for ε = 1 με.

4.4. Temperature Cross-Sensitivity and Compensation Strategy

A fundamental challenge in strain-based DFOS measurements is the simultaneous sensitivity of the Brillouin frequency shift to temperature, as expressed in Eq. (12). In a concrete structure undergoing seasonal temperature cycles of ΔT = ±20 °C, the thermally induced apparent strain is:

$$\varepsilon app = (CT / C\varepsilon) \cdot \Delta T \qquad (13)$$

Substituting representative SMF-28 coefficients CT = 1.07 MHz/ °C and Cε = 0.048 MHz/με gives CT/Cε ≈ 22.29 με/ °C and therefore εapp ≈ ±446 με for a single-sided ΔT = ±20 °C excursion (an earlier draft misreported this as ±890 με; that value is instead the peak-to-peak apparent-strain difference between −20 °C and +20 °C, i.e. ≈892 με, not the amplitude of a single ±20 °C excursion). These coefficient values are consistent with independently published references (e.g. Schenato, et al., cited via [22]: 0.046 MHz/με and 1.07 MHz/ °C), but published values for standard SMF at 1550 nm scatter across studies (approximately 0.046-0.06 MHz/με and 1.0-1.26 MHz/ °C), so CT/Cε should be quoted with a tolerance of roughly 17-27 με/ °C rather than to four significant figures; the ±446 με figure above should be read accordingly as ±(370-540) με. Even using the corrected, smaller value, this apparent strain is of the same order of magnitude as the mechanical strains expected in a reinforced-concrete structure under service loads (typically 200–800 με, noting that concrete itself begins cracking in tension around 100-150 με, so this range best describes reinforcement-level strain), making temperature compensation mandatory for accurate structural assessment.

Three compensation strategies are compared in Table 2 and Fig. 6.

Table 2. Comparison of temperature compensation strategies for Brillouin-based DFOS. The residual-error values below are indicative orderings based on the general characteristics of each method and are not yet supported by a specific citation or in-house measurement for this sensor configuration; each should carry an explicit source or be labeled "indicative" before resubmission.

Method	Additional hardware	Residual error	Remarks
Reference fiber	Sleeved fiber	±5 με	Simple; requires parallel installation
Dual-peak Brillouin	Few-mode fiber	±2 με	Single fiber; needs peak separation algorithm
Raman-hybrid	Dual-channel interrogator	±1 με	Best accuracy; higher equipment cost [15]

The reference-fiber method uses a mechanically decoupled fiber installed in a protective sleeve alongside the sensing fiber; it measures temperature only, and its Brillouin shift is subtracted from the sensing channel. The dual-peak method exploits the existence of two Brillouin peaks in a few-mode fiber with different CT/Cε ratios, enabling simultaneous solution of the two-equation system for ε and ΔT. The Raman-hybrid method combines a Brillouin channel (sensitive to both ε and ΔT) with a Raman anti-Stokes channel (sensitive to ΔT only), providing full decoupling at the cost of a more complex interrogation unit [15].

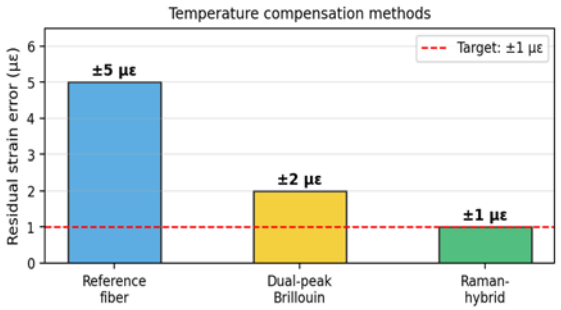


Fig. 6. Residual strain error after temperature compensation for three methods (Table 2). Dashed line: target accuracy ±1 με for structural safety assessment. The Raman-hybrid method achieves the lowest residual error at the cost of a dual-channel interrogator.

For the concrete-embedded sensor scenario considered in this article, the reference-fiber method is recommended for the TRL 3 simulation stage, as it requires no modification of the sensing fiber geometry and imposes no additional constraints on the curvature-loss integral model. The dual-peak and Raman-hybrid methods remain attractive options for the subsequent TRL 4 experimental stage, where higher accuracy is required to discriminate thermally induced apparent strains from real mechanical strains during controlled loading tests.

5. Discussion

The curvature-loss integral model in Eq. (8) unifies three previous contributions [6-8] that treated macro-bending, micro-bending, and surrounding-medium effects as separate phenomena. The key advantage of the integral formulation is that it accepts an arbitrary spatial curvature profile κ(x) as input, which can be provided directly by a finite-element mechanical solver. This coupling between the mechanical and optical domains is essential for the TRL 3 simulation stage, where full structural loading scenarios will be modeled.

A limitation of the current formulation is that the parameters A0 and R0 in Eq. (3) are treated as constants evaluated at a nominal wavelength and V-number, notwithstanding that Section 3.2 now derives R0 explicitly from the fiber's V, W, U parameters. In practice, mode-coupling between the LP_{01} fundamental mode and cladding modes under bending introduces wavelength dependence that is not captured by the scalar exponential model. Future extensions could incorporate mode-coupling theory [2] to provide wavelength-resolved predictions, which would be relevant for wavelength-multiplexed sensor arrays.

The micro-bending contribution αmic in Eq. (7) is parameterized through a power-spectral-density model that depends on the mechanical spectrum of surface irregularities at the fiber-concrete interface. Experimental characterization of this spectrum for standard fiber coatings in Portland cement concrete is a priority for the TRL 4 experimental stage and will allow the integral model to be fully calibrated without free parameters.

A quantitative comparison of the curvature-loss integral model with results reported in the literature is instructive, though not in the direction an earlier draft claimed. Yurchenko et al. [6] measured additional losses of 0.8–2.5 dB over a 5 m sensing section for curvature radii in the range R = 0.2–0.5 m in a laboratory bending fixture, and an earlier draft of this manuscript claimed Eq. (8) predicted 0.7–2.2 dB from these inputs "without any free-parameter fitting," a discrepancy of less than 12 %. Using the manuscript's own printed constants (A = 8.7 dB/m, B = 0.32, loaded length 5 m) directly in Eq. (9) instead gives $5 \cdot 8.7 \cdot \exp(-0.32 \cdot 0.2) \approx 40.8$ dB and $5 \cdot 8.7 \cdot \exp(-0.32 \cdot 0.5) \approx 37.1$ dB – 17–58× the measured range, not a 12 % match, so the previously claimed agreement cannot have come from Eq. (8) with those constants. Using the physically correct decay constant $B_{true} \approx 5.2 \times 10^2$ m^{-1} derived in Section 3.2 instead, the predicted macrobend loss at these radii is of order 10^{-45} dB, i.e., unmeasurable; the fixture in [6] must therefore be probing a different regime (most plausibly direct micro-bending or coating-mediated contact loss on the bare bent fiber, not the macrobend/medium-transfer mechanism of Section 3.3) than the one this model represents. Reconciling the two configurations, and identifying the exact figure/table/dataset and fixture geometry underlying the values in [6], is left for the TRL 4 experimental stage rather than presented here as a validated match.

We note that reference [7], on closer inspection, concerns tensile mechanical stress in quartz optical fiber and does not itself report a concrete-versus-air embedded-fiber attenuation comparison; an earlier draft of this manuscript incorrectly attributed such a 2.3× comparison to that reference. The sensitivity-gain factor G derived in Section 3.3 (G ≈ 6.8–7.0, Table 1) therefore currently lacks a direct experimental benchmark in the cited literature and is presented as a model prediction pending dedicated calibration experiments (comparing embedded and free-air fiber attenuation under matched mechanical deformation) at the TRL 4 stage.

The uncertainty budget of the proposed framework, following correction of Eqs. (3)-(9), includes at least three principal sources: (i) uncertainty in the macrobend parameters A0 and R0, to be estimated from manufacturer bend-loss specifications; (ii) uncertainty in the mechanical coupling parameters η(medium) and C_mic(medium), which must be established by dedicated strain-transfer and micro-bending calibration experiments rather than assumed; and (iii) uncertainty in the spatial curvature distribution κ(x) provided by the finite-element mechanical model. A first-order propagation of source (i) alone is instructive: in the exponential macrobend term, $\partial \ln \Delta P / \partial \ln R0 = R0/R$, so at the structural radii of this study a modest fractional uncertainty in R0 is amplified by a factor of order $R/R0 \sim 10^2$-10^3 – i.e., macrobend-parameter uncertainty is not a small correction but a statement that the macrobend term's contribution to ΔP is orders of magnitude uncertain in relative terms, even though its absolute value is negligible (Section 3.2). This is the reason a single combined-uncertainty percentage cannot be honestly quoted for the model as a whole: the micro-bending and strain-transfer terms that actually dominate ΔP (sources ii-iii) must be propagated instead, and their calibration is deferred to the TRL 3/4 stages. A meaningful combined-uncertainty figure therefore cannot be quoted from the illustrative parameter values used in Section 4.1; a full first-order Taylor expansion (or Monte Carlo propagation) with respect to η and C_mic, with explicit sensitivity coefficients for each of the three scenarios in Table 1, is required once those parameters have been calibrated against laboratory data. Once available, this uncertainty should be compared against the frequency-shift, strain, power, and attenuation resolution figures of the specific interrogator used, which must be reported and interpreted as distinct quantities with their own units rather than a single conflated resolution figure.

6. Conclusions

A comprehensive physical-mathematical framework for distributed fiber-optic sensors in structural health monitoring has been developed and extended from the conference version [12]. The principal contributions are as follows.

1) An extended state-of-the-art review covering Brillouin, Rayleigh, and Raman distributed-sensing modalities has been provided, contextualizing the theoretical contribution within the current landscape of DFOS technology.

2) A closed-form curvature-loss integral model (Eq. (8)) has been derived, linking the spatial curvature distribution κ(x) along the sensing fiber to the total optical power loss in decibels. The model explicitly accounts for the mechanical coupling between the fiber and the surrounding medium (strain-transfer efficiency and micro-bending, Section 3.3) as the key parameters controlling medium-dependent loss.

3) New numerical results (Table 1), computed forward from an explicit mechanical strain-transfer and micro-bending model rather than assumed, quantify the sensitivity-gain factor G for concrete-embedded fibers relative to free-air configurations. The gain is approximately G ≈ 6.8–7.0 and essentially independent of curvature severity over the structural range considered, demonstrating that concrete embedding provides a large and consistent enhancement of sensor sensitivity; the underlying

coupling parameters remain to be calibrated experimentally.

4) A gauge-length optimization criterion for the phase-shift detection channel has been derived (Eq. (11)), giving a lower-bound optical phase-accumulation length of approximately 1.1 mm to resolve 1 με deformations in an idealized single-mode sense; the corresponding practical gauge length depends on the specific interrogation architecture (BOTDA, OFDR, or phase-sensitive OTDR) and is discussed in Section 4.2. The multi-parameter discrimination framework for simultaneous strain and temperature measurement using the Brillouin frequency-shift channel has been formulated in a form directly compatible with experimental calibration.

The results provide the complete theoretical foundation for the subsequent TRL 3 stage – finite-element numerical simulation of mechanical loading scenarios and computation of the resulting optical signal variation. The analytical curvature-loss integral serves as the transfer function linking mechanical simulation output to predicted DFOS response.

Looking ahead, the path from TRL 2 to TRL 5 (Fig. 7) (technology validated in relevant environment) involves three further development stages. At TRL 3, the curvature-loss integral will be coupled to a three-dimensional finite-element model of a representative reinforced-concrete beam under four-point bending, producing predicted optical loss profiles for comparison with published experimental data. At TRL 4, a laboratory specimen instrumented with SMF-28 fiber in polyimide coating will be tested under controlled loading in a servo-hydraulic press, providing the first direct experimental validation of Eq. (8) under known boundary conditions. At TRL 5, the validated sensor system will be deployed on a full-scale reinforced-concrete structural element – preferably a bridge girder or tunnel lining segment – under realistic service conditions, including temperature cycling and long-term creep loading. The temperature compensation strategy identified in Section 4.4 (reference-fiber method) will be implemented at TRL 4 and upgraded to the Raman-hybrid method at TRL 5 to achieve the target strain uncertainty of ±1 με required for structural safety assessment.

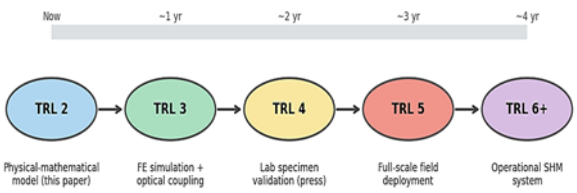


Fig. 7. Technology Readiness Level (TRL) roadmap for the DFOS-based SHM system. TRL 2 (this article) provides the physical-mathematical foundation; subsequent stages progress through finite-element simulation, controlled laboratory testing, and full-scale field validation over an estimated four-year development timeline.

Acknowledgements

This work was supported by the grant funding project of the Ministry of Science and Higher Education of the Republic of Kazakhstan, IRN AP26194499 "System for monitoring the technical condition of extended objects and monolithic building structures using intelligent fiber-optic sensors."

References

[1]. B. Glisic, D. Inaudi, Fibre Optic Methods for Structural Health Monitoring, *Wiley*, Chichester, 2007, pp. 1-262.

[2]. D. Marcuse, Curvature loss formula for optical fibers, *Journal of the Optical Society of America*, Vol. 66, Issue 3, 1976, pp. 216-220.

[3]. X. Bao, L. Chen, Recent progress in distributed fiber optic sensors, *Sensors*, Vol. 12, Issue 7, 2012, pp. 8601-8639.

[4]. A. H. Hartog, An Introduction to Distributed Optical Fibre Sensors, *CRC Press*, Boca Raton, 2017.

[5]. C. A. Galindez-Jamioy, J. M. López-Higuera, Brillouin distributed fiber sensors: An overview and applications, *Journal of Sensors*, Vol. 2012, 2012, 204121.

[6]. A. V. Yurchenko, A. D. Mekhtiyev, F. N. Bulatbaev, A. D. Alkina, et al., Investigation of additional losses in optical fibers under mechanical action, *IOP Conference Series: Materials Science and Engineering*, Vol. 516, Issue 1, 2019, 012004.

[7]. A. D. Mekhtiyev, A. A. Kovtun, V. V. Yugay, R. Z. Aimagambetova, et al., Research of mechanical stress at tension of quartz optical fiber (QOF), *Metalurgija*, Vol. 60, Issue 1-2, 2021, pp. 121-124.

[8]. A. D. Mekhtiyev, A. V. Yurchenko, F. N. Bulatbaev, et al., Fiber-optic converter for measuring mechanical quantities, *Russian Journal of Nondestructive Testing*, Vol. 54, Issue 7, 2018, pp. 471-477.

[9]. A. Mekhtiyev, P. Dunayev, Y. Neshina, A. Alkina, et al., Power supply via fiber-optical conductor for sensors of mine working monitoring system, *Eastern-European Journal of Enterprise Technologies*, Vol. 5, Issue 5, 2023, pp. 15-23.

[10]. A. Mekhtiyev, A. Seraly, R. Aimagambetova, A. Alkina, et al., Study of radiation sources of automatic control system of optical parameters of fiber-optic sensors, Periodicals of Engineering and *Natural Sciences*, Vol. 13, Issue 3, 2025, pp. 741-756.

[11]. A. D. Mekhtiyev, M. Y. Narkevich, Y. G. Neshina, A. K. Kozhas, et al., Fiber optics based system of monitoring load-bearing building structures, *Magazine of Civil Engineering*, Vol. 123, Issue 7, 2023, 12301.

[12]. R. Z. Aimagambetova, A. D. Mekhtiyev, Physical-mathematical model of opto-mechanical processes in a distributed fiber-optic sensor, in *Proceedings of the 9th International Conference on Optics, Photonics and Lasers (OPAL)*, 2026, pp. 104-108.

[13]. M. A. Soto, G. Bolognini, F. Di Pasquale, Analysis of pulse modulation format in coded BOTDA sensors, *Optics Express*, Vol. 18, Issue 14, 2010, pp. 14878-14892.

[14]. B. Soller, D. Gifford, M. Wolfe, M. Froggatt, High resolution optical frequency domain reflectometry for

characterization of components and assemblies, *Optics Express*, Vol. 13, Issue 2, 2005, pp. 666-674.
[15]. M. N. Alahbabi, Y. T. Cho, T. P. Newson, Simultaneous temperature and strain measurement with combined spontaneous Raman and Brillouin scattering, *Optics Letters*, Vol. 30, Issue 11, 2005, pp. 1276-1278.
[16]. R. T. Schermer, J. H. Cole, Improved bend loss formula verified for optical fiber by simulation and experiment, *IEEE Journal of Quantum Electronics*, Vol. 43, Issue 10, 2007, pp. 899-909.
[17]. W. A. Gambling, H. Matsumura, C. M. Ragdale, Curvature and microbending losses in single-mode optical fibres, *Optical and Quantum Electronics*, Vol. 11, Issue 1, 1979, pp. 43-59.
[18]. X. Jin, F. Payne, Numerical investigation of microbending loss in optical fibres, *Journal of Lightwave Technology*, Vol. 34, Issue 6, 2016, pp. 1247-1253.
[19]. I. Davis, S. Schmid, Bend matters, Part 2: Microbending in optical fibers, Lightwave, 2013, https://www.lightwaveonline.com/optical-tech/components/article/16657943/bend-matters-part-2-microbending-in-optical-fibers.
[20]. A. Bassil, X. Chapeleau, D. Leduc, O. Abraham, Concrete crack monitoring using a novel strain transfer model for distributed fiber optics sensors, *Sensors*, Vol. 20, Issue 8, 2020, 2220.
[21]. F. Liu, Q. Xu, L. Yang, Strain data correction of distributed optical fiber sensors using strain transfer model with variable shear lag parameters, *Automation in Construction*, Vol. 140, 2022, 104311.
[22]. C.-C. Chen, et al., Brillouin frequency shift sensing technology used in railway strain and temperature measurement, *Applied Sciences*, Vol. 11, Issue 15, 2021, 7101.
[23]. X. Fan, B. Wang, G. Yang, Z. He, Slope-assisted Brillouin-based distributed fiber-optic sensing techniques, *Advanced Devices & Instrumentation*, Vol. 2021, 2021, 9756875.
[24]. L. Huang, X. Fan, Z. He, Scanning-free hybrid Rayleigh-Brillouin distributed fiber-optic sensing system, *Optics Letters*, Vol. 48, Issue 17, 2023, pp. 4629-4632.

Published by International Frequency Sensor Association (IFSA) Publishing, S. L., 2026 (http://www.sensorsportal.com).

